ADVANCED ENERGY MATERIALS
www.advenergymat.de

Foldable Inverted Perovskite Solar Cells Enabled by Region-Dependent Microscopic and Macroscopic Strain Relaxation

Biao Zhou, Xiang Wu, Zhengyan Jiang, Jinwook Kim, Zhaojin Wang, Jiayun Sun, Ming Guan, Kai Wang, Xiaochun Liu, and Wallace C.H. Choy**

While foldable solar cells can advance the applications from emerging electronics like self-powered wearable optoelectronic devices, the poor mechanical durability of perovskite films due to the severe intrinsic strain, and the brittle nature of the flexible ITO electrode hinder foldable perovskite solar cells (F-PSCs) realization. Here, the strategy of region-dependent microscopic and macroscopic strain suppression is demonstrated to achieve efficient F-PSCs on silver nanowires (AgNWs) electrodes. Fundamentally, by introducing the region-dependent modification approach of functionalized polymer incorporation, the significant release of microscopic strain in perovskite film is demonstrated by effectively suppressing defects at places with crystallization orientation variation of perovskite surface/grain boundaries. Equally important, the gradient macroscopic strain is simultaneously eliminated by inhibiting the FA^+ (formamidinum) gradient distribution in perovskite film's depth direction. The two-strain relaxations greatly enhance the mechanical durability of perovskite film, while also improving phase stability and suppressing ion migration. Finally, efficient F-PSCs (23% PCE, the highest value among reported F-PSCs) is realized with remarkable foldability, with efficiency maintaining 94% of its initial value even after 2000 times multidirectional folding at 0.75 mm curvature radius, which far exceeds the mechanical durability of typical ITO-based flexible PSCs. This work aids in comprehending strain modulation role for F-PSCs realization.

1. Introduction

Perovskite solar cells (PSCs) are promising next-generation photovoltaic technology.[1–8] Particularly, their features like thin active layer, low-temperature solution processability, and low-cost fabrication offer the feasibility of fabricating flexible PSCs.[9,10] However, reported high-performance flexible PSCs only typically withstand bending with a curvature radius of ≈5 mm,[11–13] exhibiting limited mechanical durability. This hinders their applications in emerging electronics such as self-powered wearable and portable electronic devices, as PSCs are subjected to exceptionally harsh mechanical (external) stresses in these scenarios.[14,15] It is highly desirable to further improve the device flexibility to achieve foldable PSCs (F-PSCs) that can tolerate bending/folding cycles at extremely low curvature radii as small as 1 mm for advancing versatile applications.

B. Zhou, Z. Jiang, J. Kim, J. Sun, W. C. Choy
Department of Electrical and Electronic Engineering
The University of Hong Kong
Pokfulam Road, Hong Kong SAR 000, P. R. China
E-mail: chchoy@eee.hku.hk

X. Wu, X. Liu
Institute of Metals
College of Material Science and Engineering
Changsha University of Science and Technology
Changsha, Hunan 410004, P. R. China
E-mail: xcliu@csust.edu.cn

Z. Wang, K. Wang
Department of Electronic and Electrical Engineering
Southern University of Science and Technology
1088 Xueyuan Avenue, Shenzhen 518055, P. R. China

M. Guan
Department of Mechanical Engineering
The University of Hong Kong
Pokfulam Road, Hong Kong SAR 000, P. R. China

W. C. Choy
Materials Innovation Institute for Life Sciences and Energy (MILES)
The University of Hong Kong Shenzhen Institute of Research and Innovation
Shenzhen 518055, P. R. China

The ORCID identification number(s) for the author(s) of this article can be found under https://doi.org/10.1002/aenm.202405093

DOI: 10.1002/aenm.202405093

The severe intrinsic strain of optoelectronic devices dominantly governs mechanical durability. For PSCs, the intrinsic strain is mainly located in the perovskite active layer.[16–18] The high strain magnitude of perovskite material is particularly notable since they are among the most mechanically fragile of all photovoltaic materials.[18,19] The residual strain within perovskite films includes microscopic strain and macroscopic strain, which not only result in poor PV performances but also greatly influence the device's flexibility.[11,20] Microscopic strain is caused by the deviation of the local lattice from the ideal lattice, and it is mainly generated during perovskite film crystallization and light/bias stimulation.[21,22] For PSCs, microscopic strain represents atomic size misfit and the resulting lattice defects. Film surfaces and grain boundaries are the most susceptible locations for defects, which in turn cause microscopic strain.[18,23] This not only causes non-radiative recombination losses but also makes devices prone to crack development at localized strains when subjected to external stresses.[24] Meanwhile, solution-processed perovskite films also suffer from residual macroscopic strain that is balanced across a wide range of grains. Typically, depth-dependent macroscopic strains are formed in perovskites due to their peculiar composition and crystallization processes.[16,17] The impact of macroscopic strain on PSCs is multifaceted. For instance, the macroscopic strain within the perovskite films could lead to inferior carrier dynamics and poor operational stability.[17] According to the principles of fracture mechanics, the corresponding stress of the macroscopic strain could superimpose upon the external stress during bending/folding, resulting in the reduced fracture toughness of perovskite films,[20] decreased bearable external stress, and the enlarged bearable curvature radius of bending. Overall, both the region-dependent microscopic and macroscopic strains within perovskite films limit the flexibility/foldability of PSCs, causing cracks during bending/folding cycles and subsequent issues like ions migration, short-circuit, and moisture/oxygen invasion, and ultimately to device failure. As such, it is primarily important to eliminate the region-dependent microscopic and macroscopic strains to enhance the mechanical durability of perovskite films for realizing F-PSCs.

In this work, we demonstrate a strategy of the region-dependent microscopic and macroscopic strain suppression of perovskite films to achieve high-performance F-PSCs fabricated on substrate-integrated silver nanowires (AgNWs) electrodes. By introducing the region-dependent modification approach (RMA) of the functionalized polymer incorporation in the anti-solvent process, we suppress the microscopic strain within perovskite films by minimizing the uncoordinated Pb^{2+} defects at places with crystallization orientation variation of perovskite surfaces and boundaries. Simultaneously, we eliminate the macroscopic strain gradient along the vertical direction through the RMA-induced suppression of the FA^{+} gradient distribution in the depth direction of the perovskite film. The remarkable dual-strain relaxation greatly enhances the mechanical durability, and phase stability of perovskite films and diminishes the iodide ion migration. Benefiting from these synergistic effects of the strategy, the RMA-treated high-performance PSCs exhibit foldability (ultra-flexibility) with 94% power conversion efficiency (PCE) retention even after 2000 multidirectional folding cycles at a very small curvature radius of 0.75 mm, which is far beyond the mechanical durability of widely reported PEN/ITO or PET/ITO-based flexible PSCs.[13,25] 23% PCE is achieved for F-PSCs, which is the highest value among reported F-PSCs and ITO-free PSCs. The work contributes to comprehending the strain modulation role for realizing F-PSCs and paving the way for versatile applications of foldable perovskite devices.

2. Results and Discussion

2.1. The Release of Region-Dependent Microscopic Strain in Perovskite Films

In the formation of $FA_{1-x}Cs_xPbI_3$ perovskite films, we introduce the RMA approach of polyvinylpyrrolidone (PVP) polymer with carbonyl functional group in the antisolvent process as shown in Figure S1 (Supporting Information) to effectively modulate the adverse region-dependent microscopic and macroscopic strain. For simplicity, in the content below perovskite films (devices) without the incorporation of PVP are denoted by "control", and PVP-incorporated films (devices) are denoted by "target".

Generally, the surface of perovskite film shows high defect density which degrades device performances, and the variations of crystallization orientations are linked with high defect density and severe microscopic strain.[26] Here, we directly characterize the changes in the lattice orientations and the induced strains of the perovskites before and after RMA. The crystallinity properties of the control and target perovskite films are characterized by aberration corrected-transmission Electron Microscopy (AC-TEM) in low dose mode at a low voltage of 80 kV followed by strain analysis. The overall TEM images of cross-sectional samples are shown in Figure S2 (Supporting Information). Besides, **Figure 1**a, c shows the lattice arrangements of the surface region of the control and target samples, respectively, from which we can see the (111) and (022) crystal facets of the perovskites. Then we performed geometric phase analysis (GPA) analysis[27] on the TEM images in Figure 1a,c to obtain the corresponding strain maps as shown in Figure 1b,d (here the strain map is for y direction, Figure S3 (Supporting Information) shows the results for x direction). It is found that there is evident strain distribution in the (022) facet area for the control sample, while the target sample has no obvious strain distribution in the entire area. We also performed GPA analysis on the TEM images (still from the surface region as shown in Figure S2, Supporting Information) whose whole observed area is (111) or (022) facet, results in Figures S4, S5 (Supporting Information) show that there is no evident strain distribution for both control and target sample. These results indicate that microscopic strain within perovskite film is mainly distributed at the place where there is crystallization orientation variation,[26] and the RMA based on PVP can effectively release the region-dependent microscopic strain.

We have conducted various characterizations to study the details of the released microscopic strain. To study the interaction between PVP and perovskites, we first calculated the electrostatic potential of PVP monomer. As depicted in Figure 1e, the monomer shows the lowest electron cloud density in the carbonyl group, suggesting the feasibility of interacting with positively charged ions/defects of perovskites. From the Fourier transform infrared (FTIR) spectrometry result in Figure S6a (Supporting Information), the characteristic C═O peak of PVP shifted significantly from 1646 to 1600 cm^{-1} after mixing it with PbI_2,

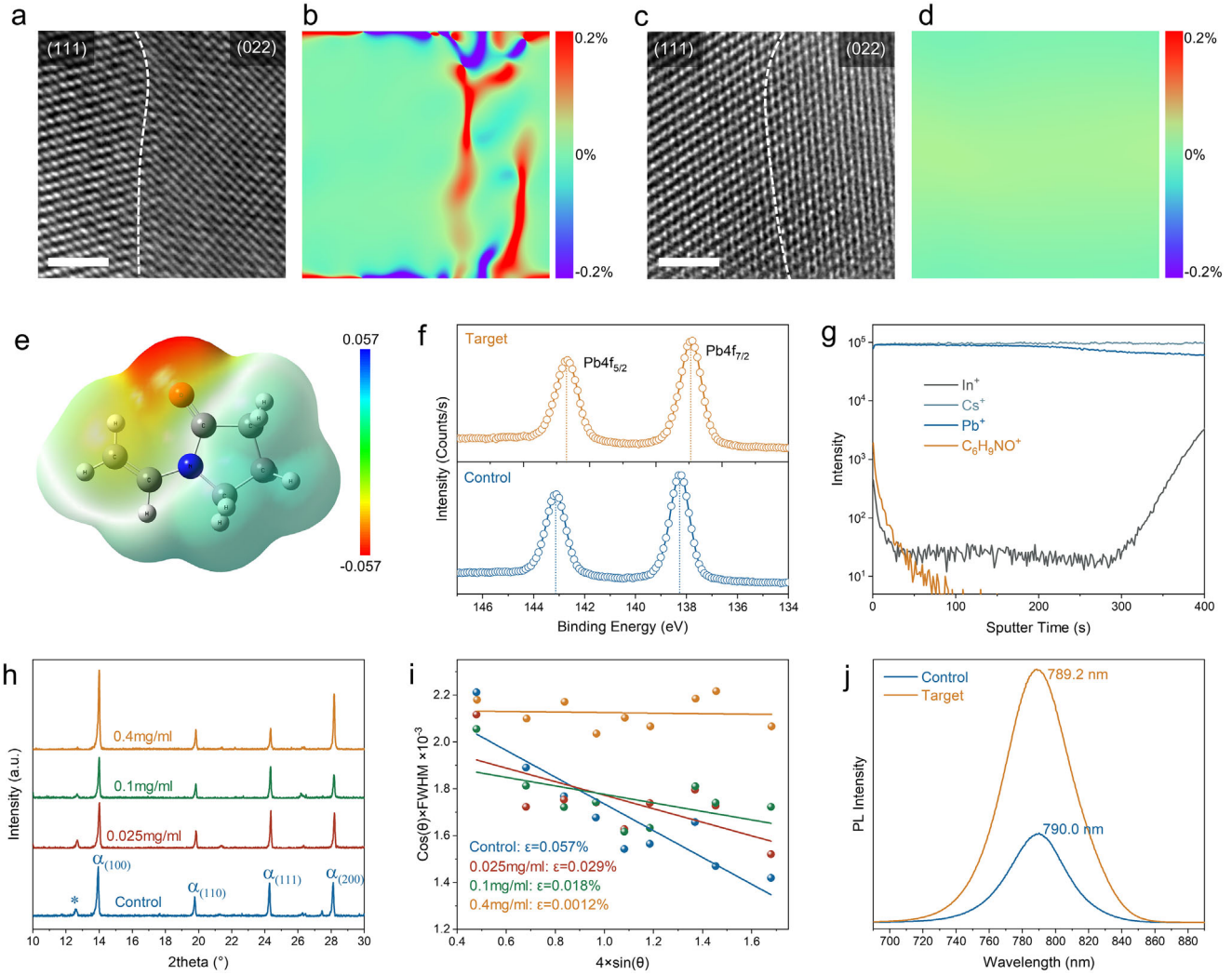

Figure 1. The release of microscopic strain in perovskite films. The TEM image collecting at the surface region of control perovskite film a) and the corresponding strain map in y direction based on the geometric phase analysis b); The TEM image collecting at the surface region of target perovskite film c) and the corresponding strain map in y direction based on the geometric phase analysis d). The part to the left of the dashed line in (a, c) is the (111) facet, and the part to the right is the (022) facet. Scale bars, 2 nm (a, c). (e) Electrostatic potential of the monomer of PVP; f) Pb 4f XPS spectra of control and target perovskite films; g) TOF-SIMS depth profiles of the PVP-treated perovskite film deposited on ITO glass ($Cs^{\pm}$ and $Pb^{\pm}$ signals are from perovskite, $C_6H_9NO^{\pm}$ signal is from PVP, and $In^{\pm}$ signal is from ITO); h) XRD patterns of control film and target films treated with different PVP concentrations. "α" for α-phase perovskite and "*" for PbI_2; i) Microscopic strain calculation by Williamson–Hall method; j) Steady-state PL spectra of control and target perovskite films.

demonstrating the strong coordination between PVP and Pb ions. X-ray photoelectron spectroscopy (XPS) results further consolidate the strong interaction between the PVP C=O group and perovskite from the shift of the Pb 4f spectrum shown in Figure 1f that the two main peaks of control film between 134 and 147 eV binding energy ascribed to the $4f_{5/2}$ and $4f_{7/2}$ orbit shift to lower binding energy after RMA (XPS spectra of $I3d_{5/2}$ are provided in Figure S6b (Supporting Information) and XPS spectra of other elements will be discussed later). Time-of-flight secondary ion mass spectrometry (TOF-SIMS) was employed to investigate the PVP distribution. It is found that PVP is mainly located at the surface than in the bulk (Figure 1g). Considering that the uncoordinated Pb^{2+} is the dominant defect in perovskite films, PVP at the surface and grain boundaries of the perovskite film can effectively passivate the uncoordinated Pb^{2+} defects at the microscopic strain distributed region by the C=O in PVP repeating units, which in turn repairs the local lattice to release microscopic strains.

We also collected the X-ray diffraction (XRD) patterns of perovskite films to study the microscopic strain. Figure 1h illustrates the XRD patterns of control and target films in which the α-phase perovskite can be observed. By gradually increasing the PVP concentration to 0.1 mg mL^{-1}, the relative diffraction intensity of the (110) facet decreases. When the concentration is further increased to 0.4 mg mL^{-1}, the (111) facet intensity also decreases and the intensity of (100) and (200) facet substantially increases. The results indicate an optimized crystal orientation and improved crystallinity. Additionally, the PbI_2 peak that

appeared in the control film gradually weakens and ultimately disappears in the target film with the increase of PVP concentration, this could be potentially beneficial for the stability of perovskite film.[28] Based on the XRD patterns in Figure 1h, the Williamson–Hall method was employed to study the microscopic strain of perovskite films (see Note S1, Supporting Information for the principles of this method). Figure 1i depicts the linear fitting of the FWHM·cosθ-4sinθ plot and the microscopic strain ε can be determined from the fitting slope. Control perovskite film exhibits severe in-plane tensile microscopic strain ($\varepsilon = 0.057\%$), while the microscopic strain of the target films treated with 0.025, 0.1, and 0.4 mg mL^{-1} of PVP solution in RMA are 0.029%, 0.018%, and 0.0012%, respectively, i.e., the microscopic strain values decreased sharply with increasing concentration. Particularly in the target film treated with 0.4 mg mL^{-1} PVP, the microscopic strain is considerably decreased by 47 times compared to the control film, thus it can be recognized that the microscopic strain in the perovskite film is completely released. The microscopic strain release suggests that the local distortion of the lattice is effectively repaired.[18] This result is consistent with the strain analysis in TEM measurements.

The defect suppression and concomitant microscopic strain release can be further confirmed by the steady-state photoluminescence (PL) and time-resolved PL of perovskite films as displayed in Figure 1j and Figure S7 (Supporting Information). The PL intensity of the target film is about three times that of the control film. The decay of TRPL fitted by a bi-exponential function (Table S1, Supporting Information) clearly shows that the target film offers a longer lifetime than that of the control film confirming the effective suppression of non-radiative recombination. In addition, Urbach energy (E_U), a commonly used parameter for assessing the electronic quality of perovskite films,[29] is calculated based on the absorption spectra. Figure S8c (Supporting Information) shows that the E_U of the target film is 8 meV lower than that of the control film which is well consistent with PL and TRPL results. Consequently, these results further support our conclusion that the effective passivation of the uncoordinated Pb^{2+} defects at the microscopic strain-distributed region of perovskite films greatly contributes to the released microscopic strain. Figure S9 (Supporting Information) shows a schematic of the microscopic strain release.

2.2. The Release of Depth-Dependent Macroscopic Strain in Perovskite Films

The distribution of macroscopic strain in the depth direction of the perovskite films before and after RMA is systematically investigated by grazing incident X-ray diffraction (GIXRD). The principle is described in Note S2 (Supporting Information) and the GIXRD parameter setting can be referred to previous study.[17] We mainly analyze GIXRD patterns of the (012) plane which is reported to provide the most dependable information on the crystal structure symmetry.[17] Three representative depths, 50, 250, and 500 nm, are chosen to represent the surface, bulk, and bottom regions of the perovskite films, respectively, and to collect the diffraction patterns. For the surface region of the control perovskite film, there is an obvious shift of the GIXRD peak to a smaller angle with the increase of the instrument tilt angle ψ (**Figure 2a**), indicating the presence of severe tensile strain. A similar trend shift is observed in the bulk and bottom regions, but the extent will decrease with the increase of the depth (Figure S10, Supporting Information). These results indicate that the order of the macroscopic strain in the depth direction is surface > bulk > bottom, implying that there is a tensile residual strain gradient in control perovskite film consistent with other reports.[17,21,30] Surprisingly, the diffraction patterns of the target perovskite film at all depths display negligible shifts in peak position with increasing ψ angle as shown in Figure 2b and Figure S10 (Supporting Information), suggesting that the macroscopic strain gradient in the depth direction is fully released. The 2θ-sin$^2\varphi$ plot based on the above diffraction patterns and corresponding fitting slopes are provided in Figure 2c to quantitatively compare the macroscopic strain of the control and target films (the macroscopic strain can be evaluated by the slope of 2θ-sin$^2\varphi$ plot, and the magnitude of strain is determined by the absolute value of the slope). The results show that the macroscopic strain at the surface, bulk, and bottom regions of the target film are reduced by a factor of 11, 9.5, and 3.2, respectively. We also measured the corresponding patterns for the (002) plane to study the distribution of macroscopic strain (Figure S11, Supporting Information), the results are consistent with that of the (012) plane that the target film with RMA is free of the gradient macroscopic strain.

Our results show that the macroscopic strain gradient along the depth direction mainly resulted from the gradient distribution of FA^+ (i.e., the composition inhomogeneity issues) and RMA can effectively solve the issue. Although inhomogeneity compositions have been reported in the solution-processed perovskite films,[16,17,31] their influence on strain is limited studied. Figure S12 (Supporting Information) illustrates the GIXRD patterns of (012) and (002) planes at different depths of the control and target films (tilt angle ψ equals 0°). The diffraction peaks of the control film shift to a smaller angle while the peak position of the target film almost remains constant when the probing depth increases. Considering that a smaller diffraction angle reflects the larger interplanar spacing d and the ionic radius of FA^+ is larger than that of Cs^+, we speculated that for the control film, the origin of the strain gradient is that there is a gradient distribution of FA^+ along the depth direction with a sequence of FA^+ content at bottom > bulk > top, while FA^+ is uniformly distributed along the depth direction for target film thus no strain gradient is observed. To prove this, we collected the cross-sectional TEM images at different regions (surface, bulk, and bottom) for control and target film to analyze the lattice heterogeneity (Figure 2d,e; Figure S2, Supporting Information). For the control film, the interplanar spacing $d_{\{012\}}$ of perovskite lattice at different regions is d_{suface}≈2.85 Å, d_{bulk}≈2.91 Å, and d_{bottom}≈2.93 Å respectively (Figure 2d), showing an increasing trend that is consistent with the proposed FA^+ distribution. In contrast, the d values of the target film are nearly identical, with d_{suface}≈2.88 Å, d_{bulk}≈2.88 Å, and d_{bottom}≈2.88 Å (Figure 2e), indicating the uniformly distributed FA^+. These results are a direct indication of lattice mismatch and concomitant strain gradient caused by FA^+ gradient distribution and the RMA leads to uniform composition and released strain gradient, supporting

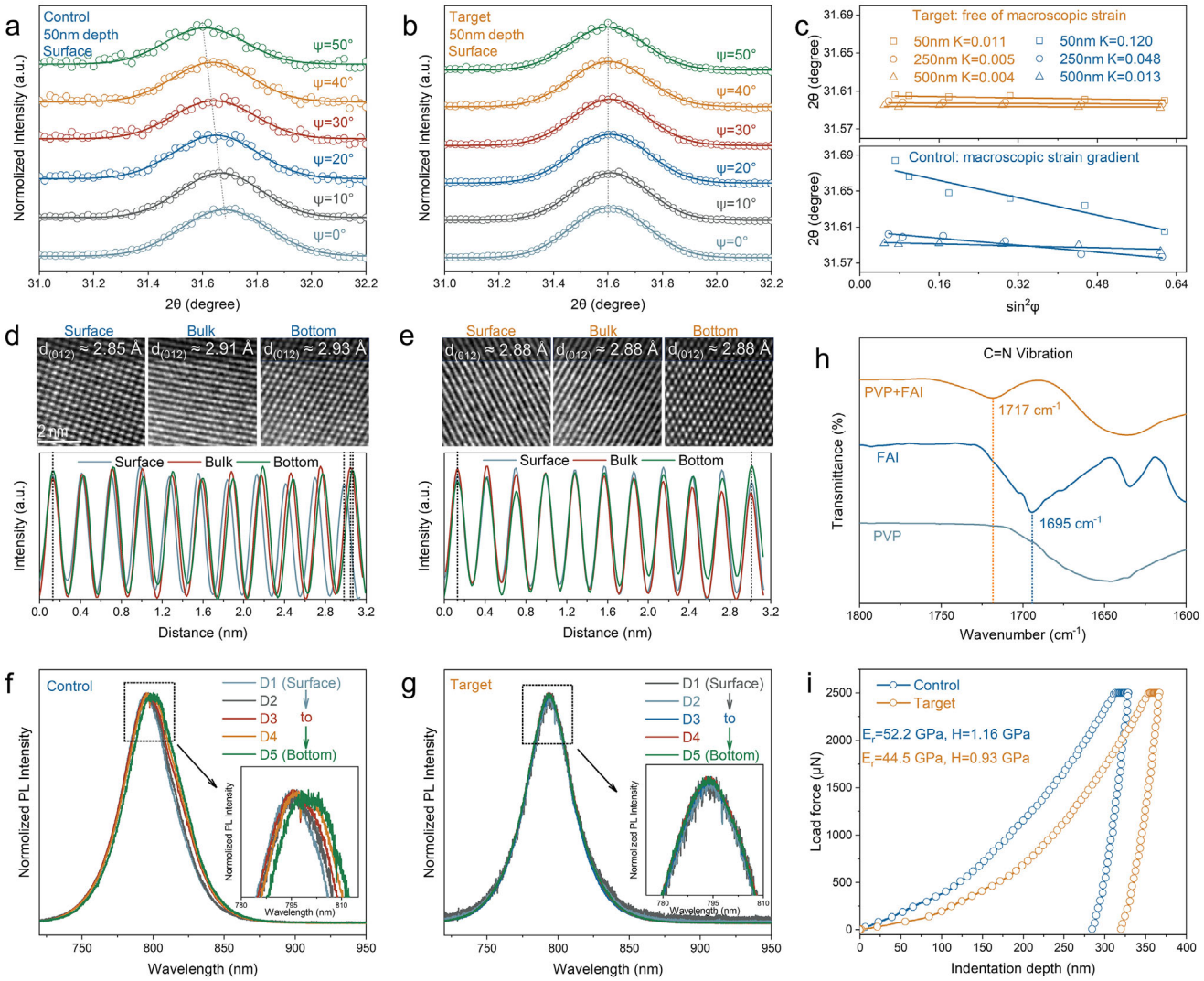

Figure 2. The release of macroscopic strain gradient in perovskite films. a) Control and b) Target perovskite films' GIXRD patterns of (012) crystal planes at different tilt angles ψ at 50 nm detection depths. c) Calculation of macroscopic strain distribution in the depth of 50, 250, and 500 nm for control and target perovskite film by classical 2θ-$\sin^2\varphi$ method. d, e) The cross-sectional TEM images from different regions of the control sample (d) and target sample (e). The cross-sectional samples were prepared with a structure of Silicon/NiO_x/2PACz/perovskite/C60. The TEM images were collected from the surface, bulk, and bottom regions of each prepared cross-sectional sample, as shown in Figure S2 (Supporting Information). The figures in the second row show the atomic intensity variations that correspond to the AC-TEM images in the first row. f, g) Confocal fluorescence microscopy PL spectra at different depths of (f) control and (g) target perovskite films, D1 to D5 means the detection depth gradually increases from the surface of the film to the bottom of the film. The film interference phenomenon shown in Figure S15 (Supporting Information) indicates that we successfully probed the deeper region of the film that is close to the bottom area; h) FTIR spectra of PVP, FAI, and the mixture of PVP and FAI; i) The loading and unloading force curves of the nanoindentation measurements for perovskite films.

our speculation. Furthermore, we conducted depth XPS analysis by using Ar^+ etching for the control and target films to investigate the Cs/N atomic ratio at different regions (Cs signal is from Cs^+ and N signal is from FA^+), related results are shown in Figures S13, S14 (Supporting Information). For Cs/N atomic ratio, the control film shows a decreasing trend while the target film shows a tiny variation when the probe region changes from surface to bottom. This is consistent with the cross-sectional TEM analysis and further validates our speculation. We also adopted a confocal fluorescence microscope to investigate the PL spectrums at different depths of the perovskite films (Figure 2f,g). Results show that there is a PL redshift in increasing the depth for the control film while the peak position of PL is insensitive to the depth in the target film. The redshift implies a narrower bandgap and an increase of FA^+ content, further supporting the gradient macroscopic strain in the control film resulting from the FA^+ gradient distribution. By introducing RMA, the constant bandgap means FA^+ in the target film is vertically uniform and thus the gradient macroscopic strain issue is addressed. Figure S16 (Supporting Information) is a schematic of the control film with a severe macroscopic strain gradient and target film free of this strain gradient.

In detail, the even distribution of FA^+ in the target film originated from the suppression of FA^+ escape during the film formation due to the interaction between PVP and FA^+. The inhomogeneous heat transfer and the FA^+ escape during thermal annealing cause the non-uniform distribution of FA^+ in perovskite films.[16,17] The FTIR spectra of PVP, FAI, and their mixture are shown in Figure 2h. The C═N characteristic peak of FAI shifted clearly from 1695 to 1717 cm^{-1} in the mixture, proving the interactions between FAI and PVP. Probably, a hydrogen bond formed between negatively charged C═O and positively charged FA^+.[32] The binding energy difference of N1s XPS spectra of control and target films also confirms this interaction (Figure S17, Supporting Information) which is further supported by the color change of the solution in Figure S18 (Supporting Information) to yellow in mixture from colorless in FAI. By using RMA, considering that PVP is distributed at the surface and grain boundaries, the uniform distribution of FA^+ in the target film should be attributed to the presence of numerous sites on the long-chain PVP that can interact with FA^+, which can help prevent the escape of FA^+ during the thermal annealing and lead to its uniform distribution. The improved compositional homogeneity is also supported by XRD results in Figure 1h; even though no extra PbI_2 is introduced into the precursor, the PbI_2 peak still exists in the control film (resulting from FA^+ escape), whereas the PbI_2 peak almost disappears in the target film for the 0.4 mg mL^{-1} case, indicating the improved film purity.

The perovskite lattice is composed of corner-sharing octahedra as well as A-site cations occupying the inter-octahedral space which causes poor mechanical properties.[20] The mechanical properties of PSCs are primarily dependent on the flexibility of perovskite films, therefore we performed nanoindentation tests to evaluate the RMA effects on the flexibility (see Figure S19 and Note S3, Supporting Information for the test details and principles). Figure 2i shows that Young's modulus E_r and hardness H of the target film exhibit a significant reduction compared to that of the control film, demonstrating RMA can effectively enhance flexibility and mechanical durability. Additionally, the reduction in Young's modulus reaffirms the effective release of the region-dependent microscopic and macroscopic strains in the perovskite film.[11]

2.3. The Impact of Strain Release on Phase Stability and Ions Migration

Phase stability is a critical issue for $FA_{1-x}Cs_xPbI_3$ perovskite,[33] we investigated phase separation by characterizing the evolution of PL spectra and diffraction patterns of perovskite films before and after illumination exposure. The spectra of the control film exhibit a redshift after illumination exposure, while the spectra of the target film show no significant shift (**Figure 3**a,b). The red shift is evidence of FA-rich phase formation because FA-rich perovskite has a lower bandgap. We also measured the diffraction patterns of perovskite films before and after illumination (Figure 3c). In the low diffraction angle region, the control film exhibits a clear δ-$CsPbI_3$ peak after illumination while the target film shows no change.[33] The results prove the formation of a Cs-rich phase in the control film (this phase is photoinactive and harmful for PSCs). Consequently, the RMA approach can effectively enhance the phase stability of perovskite film, which is contributed by the microscopic and macroscopic strain release and the long carbon chain's steric hindrance effects.

Another important issue is the halide migration in PSCs particularly the penetrated halides will react with electrode materials such as AgNWs causing device failure.[34,35] Here we evaluate the iodide migration in perovskite films by an indirect method of monitoring the resistance change of AgNWs. The resistance of the electrodes increases significantly with the elapsed time after depositing control or target perovskite film on AgNWs but the sample for the target film exhibits a lower resistance growth rate (Figure S20, Supporting Information). The change of electrode resistance with time after depositing the hole transport layer and perovskite on AgNWs is shown in Figure 3d. As time passes, the electrode resistance of the control film increases significantly, while that of the target film remains almost constant. These results reveal that the diffusion of iodides could be inhibited by the introduction of PVP into the perovskite films to a large extent. To further validate the suppressed iodide migration, we washed off the perovskite film of the aged sample in Figure S20 (Supporting Information) with DMF to expose the AgNWs and detected the elemental composition of the AgNWs by energy-dispersive X-ray spectroscopy (EDS), the related results are shown in Figures S21, S22 (Supporting Information). It is found that AgNWs obtained from the control film contain an 8.43% mass fraction of iodine while no iodine signal is detected from the AgNWs of the target film demonstrating that PVP can effectively inhibit the iodide diffusion. The release of strain can increase the activation energy of iodide migration[36], therefore, we conclude that the severe microscopic and macroscopic strains, and the severe defect at the surface and grain boundaries result in iodide ions migration in the control film, instead, most iodide ions migration can be effectively suppressed due to the RMA induced strain release and the effective defect passivation effect from PVP.

2.4. The Performances of Foldable Perovskite Solar Cells

The structure of F-PSCs on substrate-integrated AgNWs electrodes is depicted in **Figure 4**a. The statistical distribution of the photovoltaic output parameters for control and target devices is shown in Figure S23 (Supporting Information) and the champion *J–V* curves are illustrated in Figure 4b. The maximum PCE for the control device is 20.86%, with an open-circuit voltage (V_{OC}) of 1.102 V, short-circuit current density (J_{SC}) of 23.81 mA cm^{-2} and a fill factor (FF) of 79.52%. The PVP concentration is optimized to 0.4 mg mL^{-1} (Table S2, Supporting Information). It is observed that the J_{SC} does not obviously change and the PCE enhancement associated with RMA is mainly from the improvement in V_{OC} and FF. The champion F-PSCs made from the target perovskite films show a J_{SC} of 24.10 mA cm^{-2}, a V_{OC} of 1.156 V, an FF of 82.53%, and PCE of 23.00% with suppressed hysteresis (Figure S24, Supporting Information), which is the highest value reported to date for ITO-free PSCs as shown in Figure S25a (Supporting Information). The steady-state PCEs for the control and target device are 20.46% and 22.73% respectively, which are quite close to the value obtained from the *J–V* curve (Figure 4c). The integrated J_{SC} values from external quantum efficiency (EQE) spectra match well with the J_{SC} values from

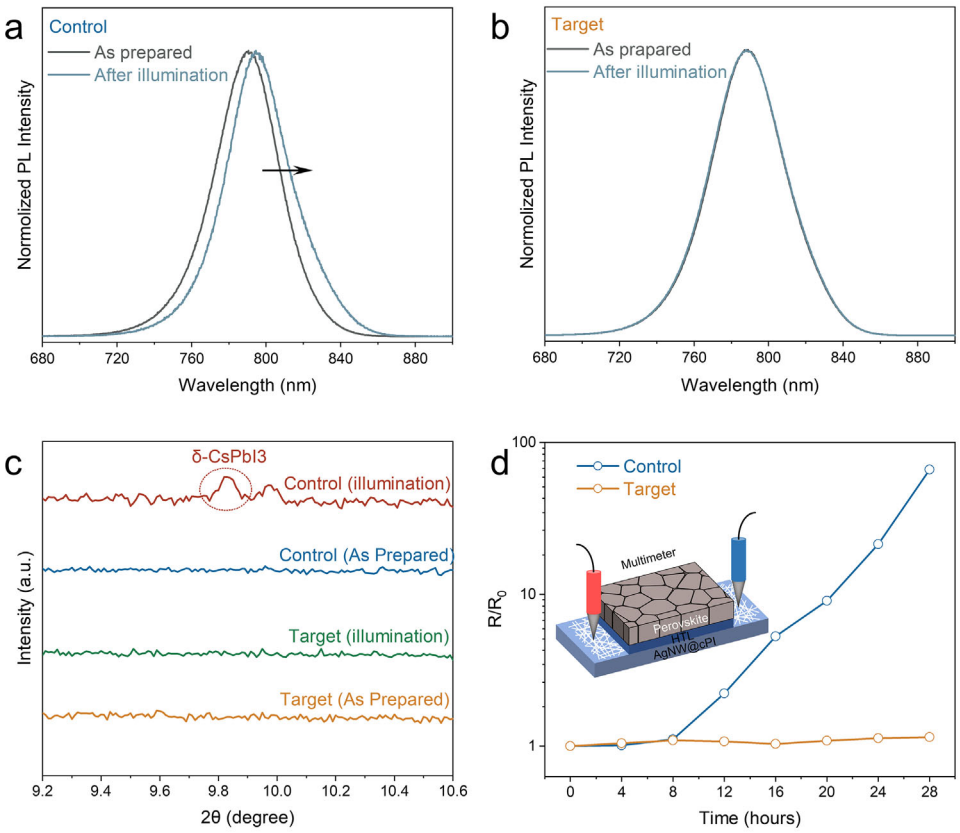

Figure 3. The impact of strain release on phase stability and ions migration. a) PL spectra of control perovskite film before and after 100 h of illumination under white LEDs; b) PL spectra of target perovskite film before and after 100 h of illumination under white LEDs; c) XRD patterns of perovskite films before and after 100 h of illumination under white LEDs; d) Variation of resistance with time after depositing HTL and perovskite films on AgNWs electrodes. The insert is a schematic of this measurement, R_0 is the initial resistance, and R is the real-time resistance. Samples are placed on a hot plate at 100 °C to accelerate the diffusion of iodide ions throughout the process.

the *J–V* curves (Figure S26, Supporting Information). For reference, we also fabricated flexible devices on PEN/ITO electrodes, and device performances are provided in Figures S27, S28 (Supporting Information).

To elucidate the improvement of V_{OC} and FF, Dark J-V is measured that the target F-PSC shows two orders of magnitude lower dark current than the control device (Figure S29a, Supporting Information). The device's ideality factor (n) of the target device is 1.093 lower than that of the control (1.287) revealing the reduced trap-assisted recombination after RMA (Figure S29b, Supporting Information). The results of electrochemical impedance spectroscopy (EIS) in Figure S29c (Supporting Information) (the insert is the equivalent circuit diagram for the Nyquist plot) show that the target exhibits a larger semicircle than the control device, indicating an enlarged recombination resistance, proving the reduced trap-assisted recombination. From the space-charge limited current (SCLC) results of hole-only devices in Figure S30 (Supporting Information), the trap-filled voltage of the control and target device is 0.84 and 0.35 V, respectively, demonstrating the effectiveness of the defect passivation brought by PVP treatment. To gain more insight into the charge carrier dynamics of the F-PSCs, we measured the transient photovoltage and transient photocurrent decay process (Figure S31, Supporting Information). Compared with the control device, the target device shows a faster photocurrent decay (from 0.86 to 0.67 µs) and a slower photovoltage decay (from 1.73 to 4.25 µs). The lower photocurrent lifetime suggests that the collection of charges is more effective due to the superior quality of the perovskite film in line with the FF improvement. The prolonged photovoltage lifetime suggests carrier recombination suppression in the device, which agrees with the increased V_{OC}. Overall, the device results further prove that RMA enables high-quality perovskite film through defect passivation, releasing strain, increasing phase stability, and suppressing ions migration, thus leading to improvement of F-PSC performances.

2.5. The Stability of Foldable Perovskite Solar Cells

The mechanical durability of our AgNWs-based F-PSCs has been investigated by performing multidirectional cyclic bending/folding tests (Movie S1, Supporting Information). Figure 4d depicts the mechanical bending stability of the control and target F-PSCs with a bending radius (R) of 5 mm. The PCE of the control device dramatically reduced to 53.8%/39.3% of the initial value after 4000 outward/inward bending cycles, while the PCE of the target device maintained at 95.1%/93.3% of the initial value even after 8000 outward/inward bending cycles. The

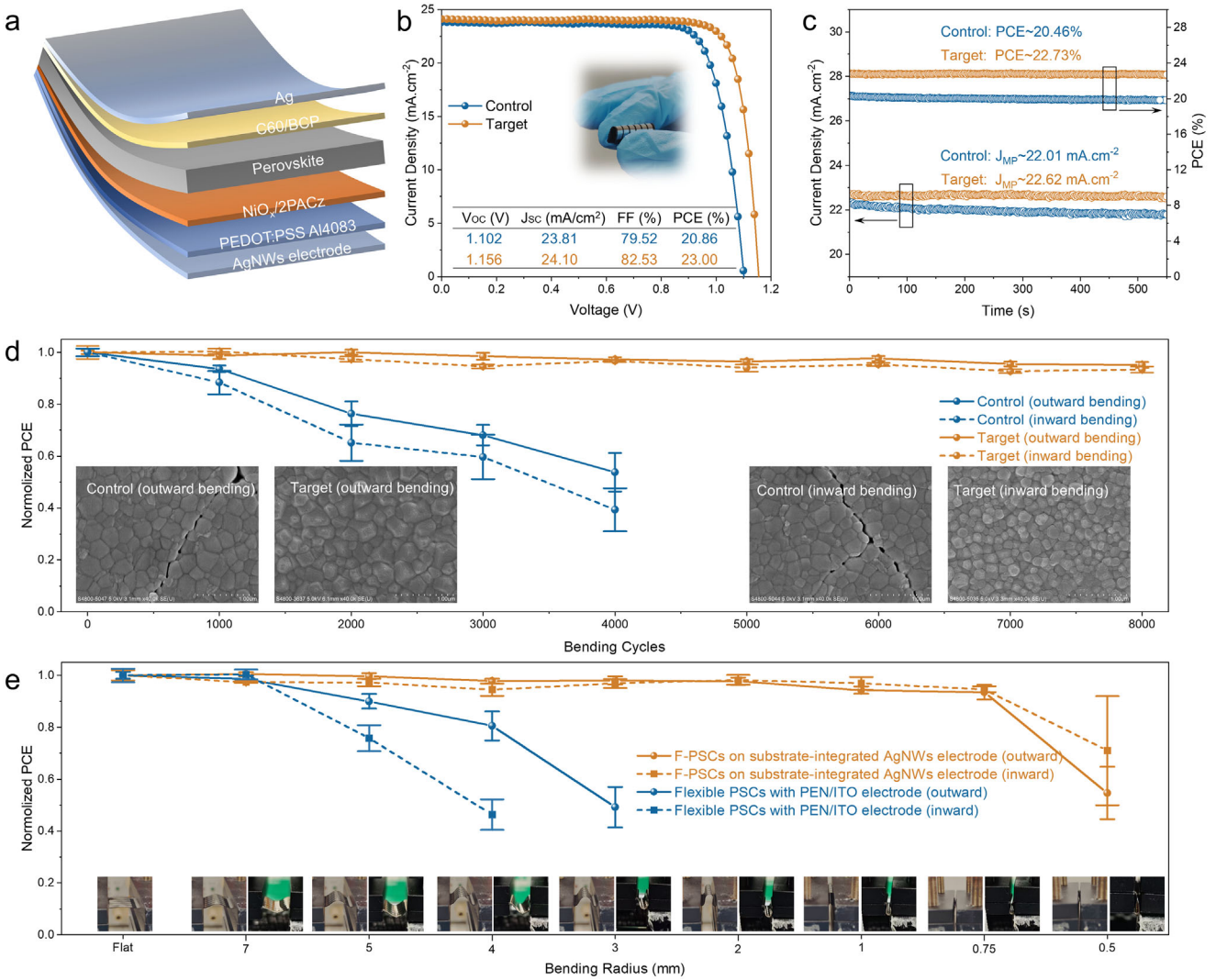

Figure 4. F-PSCs performances and their mechanical durability. a) The device structure of the F-PSCs on substrate-integrated AgNWs electrode; b) The champion *J–V* curves of the F-PSCs; c) The stable power output of the champion device; d) Performance evolution of F-PSCs on substrate-integrated AgNWs electrode as a function of multidirectional mechanical bending cycles at a bending radius of 5 mm (the inserts are the SEM images of the perovskite films from F-PSCs after 4000 bending cycles at a 5 mm curvature radius; the Ag electrode was removed by tape and C60/BCP was removed by chlorobenzene); e) Device performance evolution of F-PSCs on substrate-integrated AgNWs electrode and flexible PSCs with PEN/ITO electrode after 2000 multidirectional bending/folding cycles at different curvature radius (the inserts are photographs of F-PSCs on substrate-integrated AgNWs electrode at different bending radius including both outward and inward bending).

inserts in Figure 4d are the top-view scanning electron microscopy (SEM) images of the perovskite films of F-PSCs after 4000 multidirectional bending cycles with R of 5 mm. The transgranular crack is observed for the control film for both outward and inward conditions (The top-view SEM images of the perovskite films before bending are in Figure S32, Supporting Information) because of the presence of severe microscopic and gradient macroscopic strains in the control film, making the film a low fracture toughness and thus cracks in the cyclic bending. As expected, no crack is found in the target film due to the fully released strain, allowing it to withstand bending cycles that applied both tensile and compressive forces. For harsher stress conditions, we studied RMA-treated F-PSCs performance after 2000 multidirectional bending cycles at different curvature radii as small as 0.5 mm (Figure 4e). The degradation due to bending cycles is negligible when the curvature radius is greater than or equal to 1.0 mm. When the bending radius reduces further (i.e., $R \leq 1$ nm), it is commonly considered cyclic folding as shown in the inserts of Figure 4e. F-PSCs on substrate-integrated AgNWs electrodes can still maintain 93.5%/94.6% of their initial PCE even after 2000 outward/inward folding cycles at R = 0.75 mm, demonstrating foldability. Among reported F-PSCs, our device shows champion PCE (Figure S25b, Supporting Information). At R = 0.5 mm, the PCE drops to 54.7%/70.9% of its initial value after 2000 multidirectional folding cycles. Figure S33 (Supporting Information) shows the SEM images of the perovskite films from F-PSCs after folding at 0.5 mm. A crack is observed in this case while the AgNW electrode remains unchanged after

multidirectional cyclic folding at R = 0.5 mm (Figure S34, Supporting Information). However, the performance of RMA-treated flexible PSCs on PEN/ITO electrode starts to show a degradation as early as R = 5 mm and PCE drops to 49.2%/46.3% of the initial value at R = 3/4 mm (Figure 4e). This is consistent with previous studies that efficient flexible PSCs only withstand bending cycles at ≈R = 5 mm.[11–13] Although the perovskite film of flexible PSCs on PEN/ITO does not show any cracks (Figure S35, Supporting Information), the PEN/ITO electrode develops cracks at R = 3 mm (Figure S36, Supporting Information) and its conductivity decreases (agrees well with previous studies[13]). Consequently, the F-PSCs with RMA modification and substrate-integrated AgNWs electrode offer excellent mechanical tolerance and foldability under harsh tensile and compressive forces, which are not available in PEN/ITO-based flexible PSCs. Additionally, our F-PSCs are one-seventh the weight of flexible PSCs on PEN/ITO (Figure S37, Supporting Information), making it more advantageous for lightweight and portable applications (the power-per-weight of our foldable device and flexible PSCs on PEN/ITO is 8.15 and 1.30 W g^{-1}, respectively).

Regarding moisture and operational stability, the RMA modification can effectively enhance the resistance of perovskite films and devices to moisture-oxygen invasion. Figure S38a (Supporting Information) shows the C1s spectra, where the three main peaks of the control film correspond to C—C=O, C—N, and C—C from high to low binding energies. The C—C=O peak is related to moisture and oxygen,[37] as expected, this peak is eliminated after RMA modification, implying that the long carbon-chain polymers can effectively isolate the film from moisture and oxygen invasion. The C=O signal is not present in the control film (without any RMA modification), also confirming the successful introduction of PVP into the perovskite films. Notably, the intensity of the peak corresponding to the molecularly adsorbed H_2O (H_2O_{ad})[38] is significantly suppressed after RMA modification (Figure S38b, Supporting Information). Meanwhile, the Pb/O ratio of the target film is significantly lower than that of the control film (Figure S38c, Supporting Information). Additionally, the contact angle of water droplets on the surface of the control and target perovskite films is 64.0° and 81.1° respectively, further demonstrating the increased hydrophobic property of the target film (Figure S39, Supporting Information). With the above excellent environmental stability of target films, the stability of the unencapsulated F-PSCs in air with a relative humidity of 60% at 25 °C is studied (Figure S40a, Supporting Information). After 300-h air exposure, target F-PSCs retain 88% of their initial PCE while the control device shows rapid degradation to 47% of their initial PCE only after 90-h air exposure. The inserts show images of control and target films during the air aging process, the control film degraded quickly and became transparent while the target film remained black all the time. Regarding the maximum power point tracking (MPPT) performances of the encapsulated devices (Figure S40b, Supporting Information), control devices retained only 56.7% of the initial PCE after 700 h of operation. Differently, the target devices maintained 84.7% of the initial PCE after an even longer 920-h operation. Overall, F-PSCs with RMA modification show enhanced operational stability, which is attributed to the fully released strain, enhanced phase stability, and inhibited ion migration.

3. Conclusion

We demonstrate a facile and effective strategy to achieve efficient and foldable PSCs (including outward (tensile) and inward (compressive) folding) by introducing the region-dependent modification approach of the functionalized polymer incorporation and using homemade substrate-integrated AgNWs electrode. Particularly, we achieve the significant release of microscopic strain in the perovskite films through the effective suppression of uncoordinated Pb^{2+} defects at places with crystallization orientation variation of perovskite surfaces and boundaries. Simultaneously, we eliminate the macroscopic strain by inhibiting the FA^+ gradient depth distribution in the perovskite film. The two-strain relaxations greatly enhance the mechanical durability of perovskite film and lead to improved phase stability and suppressed ion migration. Consequently, high-performance F-PSCs with impressive flexibility (i.e., foldability) of 94% PCE retained even after multidirectional folding test at an extremely small curvature radius (R≈0.75 mm) for 2000 times have been realized, whereas such ultra-flexibility is not achievable for reported conventional ITO-based flexible PSCs. The work contributes to not only establishing the original understanding of region-dependent microscopic and macroscopic strains and their suppression but also paving the avenue of perovskite devices for applications in emerging foldable and flexible electronics.

Supporting Information

Supporting Information is available from the Wiley Online Library or from the author.

Acknowledgements

The authors thank the project of University Grant Council of the University of Hong Kong (grant No. 2302101786 and 202111159113), General Research Fund (grant Nos. 17200021, 17200823, and 17310624), Collaborative Research (grant Nos. C7035-20G) from the Research Grants Council of Hong Kong Special Administrative Region, China, and Innovation and Technology Fund (MRP/040/21X and GHP/245/22SZ) from Innovation and Technology Commission of Hong Kong Special Administrative Region, China. The authors acknowledged Prof. Mingxin Huang for help in nanoindentation tests.

Conflict of Interest

The authors declare no conflict of interest.

Data Availability Statement

The data that support the findings of this study are available from the corresponding author upon reasonable request.

Keywords

foldable perovskite solar cells, region-dependent modification, strain release

Received: October 31, 2024
Revised: February 8, 2025
Published online: March 12, 2025

[1] A. Kojima, K. Teshima, Y. Shirai, T. Miyasaka, *J. Am. Chem. Soc.* **2009**, *131*, 6050.
[2] H. Kim, C. Lee, J. Im, K. Lee, T. Moehl, A. Marchioro, S. Moon, R. Humphry-Baker, J. Yum, J E. Moser, M. Grätzel, N. Park, *Sci. Rep.* **2012**, *2*, 591.
[3] H. Zhou, Q. Chen, G. Li, S. Luo, T. Song, H. Duan, Z. Hong, J. You, Y. Liu, Y. Yang, *Science* **2014**, *345*, 542.
[4] N. J. Jeon, H. Na, E. H. Jung, T. Yang, Y. G. Lee, G. Kim, H. Shin, S. Il Seok, J. Lee, J. Seo, *Nat. Energy* **2018**, *3*, 682.
[5] M. Jeong, I. W Choi, E. M. Go, Y. Cho, M. Kim, B. Lee, S. Jeong, Y. Jo, H. W. Choi, J. Lee, J. Bae, S. K. Kwak, D. S. Kim, C. Yang, *Science* **2020**, *369*, 1615.
[6] G. Kim, H. Min, K S. Lee, D. Y Lee, S. M. Yoon, S I. Seok, *Science* **2020**, *370*, 108.
[7] J. Jeong, M. Kim, J. Seo, H. Lu, P. Ahlawat, A. Mishra, Y. Yang, M A. Hope, F T. Eickemeyer, M. Kim, Y. J. Yoon, I. W Choi, B. P. Darwich, S J. Choi, Y. Jo, J. H. Lee, B. Walker, S M. Zakeeruddin, L. Emsley, U. Rothlisberger, A. Hagfeldt, D. S. Kim, M. Grätzel, J. Y. Kim, *Nature* **2021**, *592*, 381.
[8] Z. Li, B. Li, X. Wu, S A. Sheppard, S. Zhang, D. Gao, N J. Long, Z. Zhu, *Science* **2022**, *376*, 416.
[9] J. Zhang, W. Zhang, H. Cheng, S. R. P. Silva, *Mater. Today* **2020**, *39*, 66.
[10] Y. Y. Kim, T. Yang, R. Suhonen, A. Kemppainen, K. Hwang, N. J. Jeon, J. Seo, *Nat. Commun.* **2020**, *11*, 5146.
[11] X. Wu, G. Xu, F. Yang, W. Chen, H. Yang, Y. Shen, Y. Wu, H. Chen, J. Xi, X. Tang, Q. Cheng, Y. Chen, X. Ou, Y. Li, Y. Li, *ACS Energy Lett.* **2023**, *8*, 3750.
[12] Z. Dai, S. Li, X. Liu, M. Chen, C E. Athanasiou, B W. Sheldon, H. Gao, P. Guo, N P. Padture, *Adv. Mater.* **2022**, *34*, 2205301.
[13] K. Huang, Y. Peng, Y. Gao, J. Shi, H. Li, X. Mo, H. Huang, Y. Gao, L. Ding, J. Yang, *Adv. Energy Mater.* **2019**, *9*, 1901419.
[14] Z. Li, S. Wu, J. Zhang, K. C Lee, H. Lei, F. Lin, Z. Wang, Z. Zhu, A K. Y. Jen, *Adv. Energy Mater.* **2020**, *10*, 2000361.
[15] J. Min, S. Demchyshyn, J. R. Sempionatto, Y. Song, B. Hailegnaw, C. Xu, Y. Yang, S. Solomon, C. Putz, L. E. Lehner, J. F. Schwarz, C. Schwarzinger, M. C. Scharber, E. S. Sani, M. Kaltenbrunner, W. Gao, *Nat. Electron.* **2023**, *6*, 630.
[16] X. Hu, C. Zhu, W. Zhang, H. Wang, J. Wang, F. Ren, R. Chen, S. Liu, X. Meng, J. Zhou, Y. Pan, X. Tian, D. Sun, S. Zhang, Y. Zhang, Z. Liu, Q. Chen, W. Chen, *Nano Energy* **2022**, *101*, 107594.
[17] C. Zhu, X. Niu, Y. Fu, N. Li, C. Hu, Y. Chen, X. He, G. Na, P. Liu, H. Zai, Y. Ge, Y. Lu, X. Ke, Y. Bai, S. Yang, P. Chen, Y. Li, M. Sui, L. Zhang, H. Zhou, Q. Chen, *Nat. Commun.* **2019**, *10*, 815.
[18] D. Liu, D. Luo, A N. Iqbal, K W. P. Orr, T A. S. Doherty, Z. Lu, S D. Stranks, W. Zhang, *Nat. Mater.* **2021**, *20*, 1337.
[19] B. L. Watson, N. Rolston, A. D. Printz, R. H. Dauskardt, *Energy Environ. Sci.* **2017**, *10*, 2500.
[20] Q. Dong, M. Chen, Y. Liu, F T. Eickemeyer, W. Zhao, Z. Dai, Y. Yin, C. Jiang, J. Feng, S. Jin, S. Liu, S. M. Zakeeruddin, M. Grätzel, N. P. Padture, Y. Shi, *Joule* **2021**, *5*, 1587.
[21] G. Yuan, W. Xie, Q. Song, S. Ma, Y. Ma, C. Shi, M. Xiao, F. Pei, X. Niu, Y. Zhang, J. Dou, C. Zhu, Y. Bai, Y. Wu, H. Wang, Q. Fan, Q. Chen, *Adv. Mater.* **2023**, *35*, 2211257.
[22] D. Kim, J. S. Yun, P. Sharma, D. S. Lee, J. Kim, A. M. Soufiani, S. Huang, M. A. Green, A. W. Y. Ho Baillie, J. Seidel, *Nat. Commun.* **2019**, *10*, 444.
[23] R. Wang, J. Xue, K. Wang, Z. Wang, Y. Luo, D. Fenning, G. Xu, S. Nuryyeva, T. Huang, Y. Zhao, J. L. Yang, J. Zhu, M. Wang, S. Tan, I. Yavuz, K N. Houk, Y. Yang, *Science* **2019**, *366*, 1509.
[24] T. W. Jones, A. Osherov, M. Alsari, M. Sponseller, B. C. Duck, Y.-K. Jung, C. Settens, F. Niroui, R. Brenes, C. V. Stan, Y. Li, M. Jalebi, N. Tamura, J. E. Macdonald, M. Burghammer, R. H. Friend, V. Bulovic, A. Walsh, G. J. Wilson, S. Lilliu, S. D. Stranks, *Energy Environ. Sci.* **2019**, *12*, 596.
[25] Y. Wu, G. Xu, J. Xi, Y. Shen, X. Wu, X. Tang, J. Ding, H. Yang, Q. Cheng, Z. Chen, Y. Li, Y. Li, *Joule* **2023**, *7*, 398.
[26] S. Jariwala, H. Sun, G W. Adhyaksa, A. Lof, L A. Muscarella, B. Ehrler, E C. Garnett, D S. Ginger, *Joule* **2019**, *3*, 3048.
[27] M. Hÿtch, E. Snoeck, R. Kilaas, *Ultramicroscopy* **1998**, *74*, 131.
[28] Y. Zhao, F. Ma, Z. Qu, S. Yu, T. Shen, H. Deng, X. Chu, X. Peng, Y. Yuan, X. Zhang, J. You, *Science* **2022**, *377*, 531.
[29] H. Mehdizadeh-Rad, J. Singh, *ChemPhysChem* **2019**, *20*, 2712.
[30] Z. Zheng, F. Li, J. Gong, Y. Ma, J. Gu, X. Liu, S. Chen, M. Liu, *Adv. Mater.* **2022**, *34*, 2109879.
[31] S. P. Harvey, Z. Li, J. A. Christians, K. Zhu, J. M. Luther, J. J. Berry, *ACS Appl. Mater. Interfaces* **2018**, *10*, 28541.
[32] S. Wu, S. Lin, Z. Shi, D. Guo, H. Huang, X. Zhou, D. Zhang, K. Zhou, W. Zhang, Y. Hu, C. Zhou, *Small* **2023**, *19*, 2207848.
[33] N. Li, Y. Luo, Z. Chen, X. Niu, Xiao. Zhang, J. Lu, R. Kumar, J. Jiang, H. Liu, X. Guo, B. Lai, G. Brocks, Q. Chen, S. Tao, D. P. Fenning, H. Zhou, *Joule* **2020**, *4*, 1743.
[34] Y. Xu, Z. Lin, W. Wei, Y. Hao, S. Liu, J. Ouyang, J. Chang, *Nanomicro Lett* **2022**, *14*, 117
[35] A. Kim, H. Lee, H. Kwon, H. S. Jung, N. Park, S. Jeong, J. Moon, *Nanoscale* **2016**, *8*, 6308.
[36] Z. Li, X. Li, X. Chen, X. Cui, C. Guo, X. Feng, D. Ren, Y. Mo, M. Yang, H. Huang, R. Jia, X. Liu, L. Han, S. Dai, M. Cai, *Joule* **2023**, *7*, 1363.
[37] M. Li, R. Sun, J. Chang, J. Dong, Q. Tian, H. Wang, Z. Li, P. Yang, H. Shi, C. Yang, Z. Wu, R. Li, Y. Yang, A. Wang, S. Zhang, F. Wang, W. Huang, T. Qin, *Nat. Commun.* **2023**, *14*, 573.
[38] C. Ma, F T. Eickemeyer, S. Lee, D. Kang, S. J. Kwon, M. Grätzel, N. Park, *Science* **2023**, *379*, 173.